Reconstruction of Propagated Electrical Activity with a Two-Dimensional Model of Anisotropic Heart Muscle

Fernand A. Roberge, Alain Vinet, and Bernard Victorri

From the Institute of Biomedical Engineering, École Polytechnique and Faculty of Medicine, Université de Montréal, Montréal (Québec), Canada

SUMMARY. The propagated electrical activity in normal anisotropic cardiac muscle is characterized by directionally dependent variations in the rising phase of the action potential. An important question concerns the relation between such variations and the propagation velocity and extracellular potentials. This problem was studied here in a sheet of cells, under conditions of uniform intracellular anisotropic resistivity and constant electrical membrane properties, through a numerical solution of the two-dimensional propagation equation. The numerical solution implies a lumping of the cytoplasmic and intercellular resistances into an equivalent junctional resistance to form a distributed resistive network representing the intracellular domain. The interstitial space is assumed isotropic and unbounded, with a resistivity of 100 $\Omega \cdot$cm. The electrical properties of the cell membrane are represented by a Beeler-Reuter model. The stimulus current is applied to a small area of the sheet, and attention is focussed on the stable propagated events occurring some 5 or 6 length constants away from the stimulation site. The numerical solution is a good approximation of a continuous uniform structure when the cell size is less than 10% of the length constant along both major axes. Conditions of non-uniform propagation, with directionally dependent variations in the maximum rate of rise and time constant of the foot of the action potential were simulated by increasing the cell size to 30% of the length constant in the transverse direction of the sheet. Our results indicate that the directional changes in the maximum rate of rise correspond to small modifications of the extracellular potentials, while the directional changes in time constant of the foot are associated with the propagation velocity. The maximum effects are observed along the transverse direction as follows: a 19% increase in maximum rate of rise corresponds to a decrease of about 6% in the peak-to-peak amplitude of the extracellular potential, and a 24% increase in time constant of the foot is associated with a decrease of about 7% in the propagation velocity. Under the conditions of the present study, however, the simulated directional changes in maximum rate of rise are smaller than those experimentally observed so the corresponding changes in the extracellular potentials are probably underestimated. (*Circ Res 58: 461-475, 1986*)

Downloaded from http://ahajournals.org by on March 12, 2022

THE electrotonic spread of current from cell to cell in heart muscle shows the existence of an effective axial resistance in the direction of propagation (Woodbury and Crill, 1961). This resistance includes the composite effect of the cytoplasmic resistivity, the resistance and distribution of cell-to-cell connections, and the relative volume of the intracellular and interstitial space. In two-dimensional anisotropic cardiac muscle, the effective axial resistance is lowest along the longitudinal axis of the cells, where the propagation velocity is maximum, and largest in the transverse direction, where the propagation velocity is minimum (Clerc, 1976; Roberts et al., 1979; Spach et al., 1981). Clerc (1976) has concluded that the disparity in propagation velocity can be explained on the sole grounds of differences in the resistivity of the intracellular and interstitial paths for current flow in the two directions, and that the shape of the action potentials is the same throughout the tissue. Under these conditions, it can be argued that continuous medium theory is applicable to two-dimensional cardiac muscle, as Hodgkin (1954) has proposed for one-dimensional propagation in nerve.

However, this suggestion can be disputed, since deviations from the continuous medium theory were reported by Spach et al. (1981), who showed, under conditions in which the membrane properties remained constant, that the rising phase of the action potential is different along the slow axis compared to the fast axis. The most conspicuous alterations likely to affect propagation were an increase of the maximum rate of rise of the action potential ($\dot{V}_{max}$) and a decrease in the time constant of the foot (τ_{foot}), along directions other than longitudinal. It was proposed that such changes in the shape of depolarization can be accounted for by recurrent discontinuities in intracellular resistance in the transverse direction which cause propagation to be discontinuous on a microscopic scale.

As a result of these observations, there is some uncertainty as to the appropriateness of using continuous medium theory to describe the propagation of electrical activity in a thin sheet of anisotropic cardiac muscle. An important question concerns the relation between variations in the value of $\dot{V}_{max}$ and τ_{foot} according to the direction of propagation (directional variations in $\dot{V}_{max}$ and τ_{foot}) and the propagation velocity and extracellular potentials. This question is the principal concern of the present paper and is addressed by means of a model study based on a numerical solution of the two-dimensional propagation equation. This numerical solution is equivalent to considering a sheet of cells as a distributed electrical circuit incorporating a suitable representation of the cell membrane properties.

The simulation study was carried out under conditions of uniform intracellular anisotropic resistivity and constant electrical membrane properties in order to delineate clearly the effects due to directional changes in the rising phase of the action potential. As a first step we obtain a numerical solution for the case of uniform propagation, where the rising phase of the propagated action potential is the same in all directions. Next we examine a numerical approximation of the effects of directional changes in $\dot{V}_{max}$ and τ_{foot} on the propagation velocity and extracellular potentials. The nature and magnitude of these effects are compared to the case of uniform propagation and are discussed in relation to relevant experimental observations in cardiac tissue.

Methods

We consider a thin, uniformly anisotropic section of myocardium which can be characterized as two-dimensional (i.e., there is no current flow in the third dimension). We assume that the cells have a constant surface-to-volume ratio, S_v. They are electrically coupled such that the combination of cytoplasmic and intercellular resistances produces a net longitudinal intracellular resistivity, $\rho_x(\Omega\cdot cm)$, and a transverse intracellular resistivity, $\rho_y(\Omega\cdot cm)$. The interstitial medium is assumed isotropic and unbounded, each cell being essentially in full contact with a large body of perfusing fluid. As a result, the extracellular resistivity, $\rho_e(\Omega\cdot cm)$, is much lower than ρ_x or ρ_y, and the magnitude of the extracellular potential, $\phi_e(mV)$, is small enough so that the intracellular potential may be assumed to be equal to the transmembrane potential V(mV).

Continuous Two-Dimensional Model

The equation describing propagation in a continuous and uniform thin sheet model corresponds to a simplification of the general solution for a two-dimensional anisotropic bisyncytium, assuming equal interstitial and intracellular anisotropy ratios (Plonsey and Barr, 1984). This equation is applicable here since the small value of ρ_e is consistent with the assumption of equal intracellular and extracellular anisotropy ratios (Plonsey and Rudy, 1980). Briefly, the equation is obtained by applying Ohm's law to the intracellular milieu to express the intracellular current density. The transmembrane current is derived by taking the divergence of the intracellular current density. Division by the surface-to-volume ratio of the cell (S_v) allows us to express the transmembrane current per unit area of membrane, $I_m(\mu A/cm^2)$. In the reference system aligned with the principal axes of the resistivity tensor,

$$I_m = \frac{1}{S_v}\left(\frac{1}{\rho_x}\frac{\partial^2 V}{\partial x^2} + \frac{1}{\rho_y}\frac{\partial^2 V}{\partial y^2}\right) \tag{1}$$

This expression must equal the sum of capacitive and ionic transmembrane current components to yield the two-dimensional propagation equation:

$$\lambda_x^2\frac{\partial^2 V}{\partial x^2} + \lambda_y^2\frac{\partial^2 V}{\partial y^2} = \tau_m\frac{\partial V}{\partial t} + R_m I_{ion} \tag{2}$$

in which

$$\begin{aligned}\lambda_x &= (R_m/\rho_x S_v)^{1/2};\\ \lambda_y &= (R_m/\rho_y S_v)^{1/2};\\ \tau_m &= R_m C_m\end{aligned} \tag{3}$$

where C_m, R_m and I_{ion} are, respectively, the membrane capacitance, the membrane resistance at rest, and the ionic current, all per unit area of membrane.

Equation 2 will be solved numerically in a nearly exact manner to describe the two-dimensional propagation in a continuous and uniformly anisotropic sheet (sheet A in the sequel). As indicated in the Appendix, there are several features that should be displayed by the solution of Equation 2 and which are expected to characterize a continuous uniformly anisotropic sheet. Activation from a point source produces elliptical isochrones and, for steady state propagation, the velocity profile is also elliptical (Eq. A.4). Along a given radial direction, at an angle β with the cell's longitudinal axis (see Fig. 9), one can consider an arbitrary resistivity, $\vec{\rho}_\beta$ (Eq. A.7), corresponding to the ray velocity $\vec{\theta}_\beta$. The ratio of the actual ($\vec{\theta}_\beta$) and subthreshold ($\vec{\theta}_{0\beta}$) conduction velocities is constant in any given direction (Eq. A.14). Similarly, the time constant of the foot of the action potential, τ_{foot}, is constant throughout the sheet (Eq. A.15). In fact, $\vec{\theta}_\beta$ is approximately proportional to the inverse square root of the resistivity ($\vec{\rho}_\beta$) in the direction of propagation (Eq. A.17).

The Results will show that all the above characteristics are exhibited by our continuous, uniformly anisotropic, sheet model (sheet A). In addition, it was verified that the shape of the propagating action potential is constant throughout sheet A. Therefore, this model can be considered as a good approximation of a continuous two-dimensional medium and may be used to calculate the corresponding extracellular potentials (using Eq. 8 below).

Numerical Sheet Model

Equation 2 can be written in dimensionless form as:

$$\frac{\partial^2 W}{\partial \bar{x}^2} + \frac{\partial^2 W}{\partial \bar{y}^2} = \frac{\partial W}{\partial \bar{t}} + R_m I_{ion} \tag{4}$$

with

$$\begin{aligned}&\bar{x} = x/\lambda_x;\ \bar{y} = y/\lambda_y;\ \bar{t} = t/\tau_m;\\ &W(\bar{x}, \bar{y}, \bar{t}) = V(x, y, t)\end{aligned} \tag{5}$$

To solve Equation 4 numerically, with a von Neumann boundary condition ($\nabla\vec{W} = 0$), we calculate the potential values over a rectangular grid superposed on the sheet surface. Each point on the grid is made to coincide with the nodes of the equivalent network of Figure 1B, so that the internodal distances are Δx and Δy along each axis. $W_{i,j}$ is the potential of node i, j at a given time instant,

Downloaded from http://ahajournals.org by on March 12, 2022

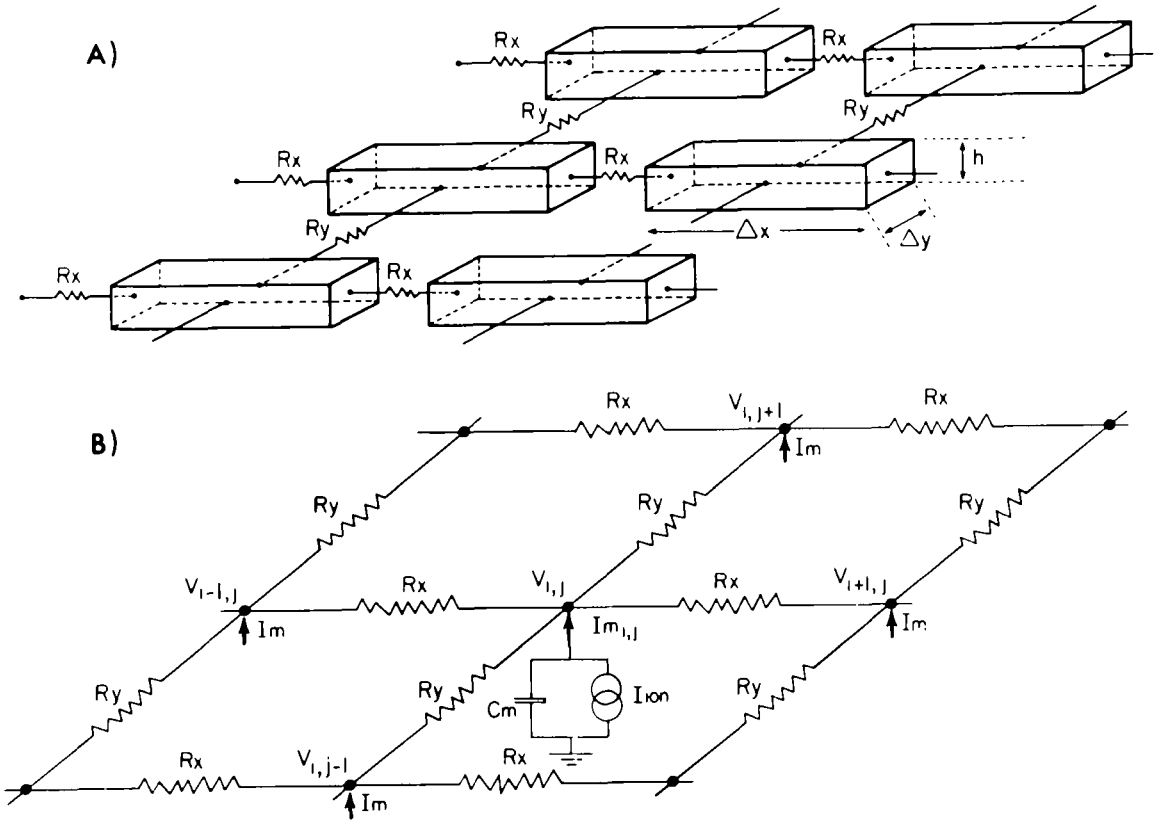

FIGURE 1. *Diagrammatic representation of a symmetrical sheet model. Panel A: each volume element, V_S, is depicted as a small parallelepiped of length Δx, width Δy, and thickness h. The combined cytoplasmic and junctional resistances are represented by Rx in the longitudinal direction and Ry in the transverse direction. These resistances reflect, respectively, the net axial resistivities ρ_x and ρ_y defined in the text. Panel B: distributed equivalent electric network in which the surface membrane of each volume element is represented by a Hodgkin-Huxley model diagrammed as a capacitance, C_m, in parallel with an ionic current source, I_{ion}. I_m is the total cell membrane current of a volume element entering at each node. $V_{i,j}$ is the transmembrane potential of element (or node) i, j*

with i and j corresponding to the x and y directions respectively. Equation 4 can be written as a difference equation:

$$\frac{(W_{i-1,j} - 2W_{i,j} + W_{i+1,j})}{\Delta \bar{x}^2} + \frac{(W_{i,j-1} - 2W_{i,j} + W_{i,j+1})}{\Delta \bar{y}^2} = \frac{\partial W_{i,j}}{\partial \bar{t}} + R_m I_{ion}. \quad (6)$$

We rewrite Equation 6 in the original coordinate system for a volume element V_S. In so doing we introduce a superscript to indicate time, with $V^t_{i,j}$ being the membrane potential of element i, j at time t. We approximate $\frac{\partial V}{\partial t}$ as a forward difference, $(V^{t+\Delta t}_{i,j} - V^t_{i,j})/\Delta t$. We replace the second central difference (see Crank and Nicholson, 1947) with the average of the second central difference at time t and at time t + Δt, and rearrange to

$$\begin{aligned} &K_1 V^{t+\Delta t}_{i-1,j} + K_2 V^{t+\Delta t}_{i,j-1} - (2K_1 + 2K_2 + 1)\, V^{t+\Delta t}_{i,j} \\ &+ K_1 V^{t+\Delta t}_{i+1,j} + K_2 V^{t+\Delta t}_{i,j+1} = -K_1(V^t_{i-1,j} + V^t_{i+1,j}) \\ &- K_2(V^t_{i,j-1} + V^t_{i,j+1}) + (2K_1 + 2K_2 - 1)V^t_{i,j} \\ &+ \frac{\Delta t}{C_m} I_{ion\,i,j} \end{aligned} \quad (7)$$

where $K_1 = \Delta t/(2\rho_x C_m S_v \Delta x^2)$ and $K_2 = \Delta t/(2\rho_y C_m S_v \Delta y^2)$ for each element i, j. This has the general form whereby the left-hand side can be easily solved at each time step for $V^{t+\Delta t}_{i,j}$ for i, j = 1, 2, . . . by matrix techniques provided that we calculate $I^{t+\Delta t}_{ion}$ from quantities known at time t. A similar solution for the one-dimensional case has been described by Joyner et al. (1984).

It can be shown, using basic circuit theory principles, that Equation 7 applies also to the electrical circuit diagram depicted in Figure 1B which can then be considered as a numerical sheet model of cardiac tissue. As illustrated in Figure 1A, each cell can now be defined as a volume element, V_s, of length Δx width Δy and thickness h. The shape of the cell model is arbitrary and is chosen here as a rectangular parallelepiped purely for convenience. The combined cytoplasmic and junctional resistances are represented as a single equivalent resistance located at the junction between adjacent cells, R_x in the longitudinal direction and R_y in the transverse direction. In consequence, each cell model has a zero cytoplasmic resistance and its membrane potential is uniform at any given time instant. Each isopotential cellular volume element, V_s, is identifiable with a given node $(V_{i,j})$ of the corresponding electrical network, Figure 1B. The cell membrane properties are represented by a Beeler-Reuter (1977) model producing the membrane current entering at each node.

As can be appreciated from Equation 6, the accuracy of the numerical approximation depends solely upon the values of $\Delta \bar{x}$ and $\Delta \bar{y}$ (referred to as discretization factors

Downloaded from http://ahajournals.org by on March 12, 2022

in the sequel) which are defined as the ratio of the cell size to the length constant (see Eq. 5). Low values of $\Delta\bar{x}$ and $\Delta\bar{y}$ allow a greater accuracy, that is an approximation which is closer to the continuous case (Eq. 2), but require a correspondingly larger computation time. In practice, we have found that a discretization factor of 0.1 in both directions gives a good approximation of the continuous case (see Results). In comparison, a numerical solution with a discretization factor of 0.2 apparently provides an acceptable approximation in the one-dimensional case (Joyner, 1982).

For the specific calculations being done here, where there is an interface between anisotropic tissue and a uniform isotropic extracellular volume conductor, there is a large smearing effect on the potentials which makes the assumption of extracellular isotropy valid for the calculation of extracellular potentials near the surface of the tissue (Geselowitz et al., 1982). Then it is reasonable to regard the sheet model as representing a very thin layer of tissue, essentially one-cell thick. Here the extracellular potential, ϕ_e, is calculated for a sheet of thickness h as illustrated in Figure 1A. Using the value of I_m entering at each node (Fig. 1B), one can calculate ϕ_e in a volume conductor of homogeneous resistivity, ρ_e, as follows (Plonsey, 1969; Spach et al., 1979):

$$\phi_e(P) = \frac{\rho_e}{4\pi} \sum_{i=1}^{M} \sum_{j=1}^{N} \frac{I_{mi,j}}{r_{i,j}} V_s \qquad (8)$$

where M and N are the total numbers of volume elements along x and y, respectively, $r_{i,j}$ is the distance from the observation point, P, to the center of the volume element V_s at node i, j. It should be noted that ϕ_e cannot be expressed solely as a function of $\bar{x}$, $\bar{y}$, W, and thus depends explicitly on the chosen values of Δx, Δy, ρ_x, ρ_y.

Equation 8 implies each element to be a point source in a uniform medium of infinite extent. In practice, under the conditions of the present study, the exponential characteristics of the action potential upstroke (see Results) lead to membrane currents which tail off exponentially either with time or distance. Then the summations of Equation 8 involve a fairly limited number of volume elements. Therefore, the computation of ϕ_e is restricted to a rather small area of the sheet so border effects can be avoided. This situation is sufficiently comparable to the extracellular potential recorded from a sheet of tissue lying in a superfusion chamber.

Computer Simulation

Solutions to Equations 7 and 8 were programmed in FORTRAN on a CYBER 835 digital computer (Control Data Corporation). In the initial phase of the program the sheet parameters are set up, with computation of K_1 and K_2. At each time step, the function $I_{ion(i,j)}$ is evaluated for each element using the ventricular model of Beeler and Reuter (1977), and used to compute the array on the right-hand side of Equation 7. The matrix formed by Equation 7 is then solved for $V_{i,j}^{t+\Delta t}$ for i, j = 1, 2, . . . The resulting system's matrix is pentadiagonal and its inversion is computationally expensive. To obtain a rapidly converging solution, we used the Gauss-Seidel iterative method (Forsythe and Wasow, 1960).

Ionic currents are computed at each time step using the hybrid integration method (Moore and Ramon, 1974; Drouhard and Roberge, 1982a). This method assumes that the gating variable equations are linear for sufficiently small changes in the membrane potential, so that the equations can be solved explicitly over the corresponding time increment. An automatic procedure is normally used to adjust the time increment so that the membrane potential offset remains between arbitrary predetermined limits (Victorri et al., 1985). Here, the computation involves mainly the rising phase of the action potential some 20 msec into the plateau phase. Under these conditions, there is always a subgroup of units in the process of rapid depolarization and a time increment no greater than 0.032 msec must be used.

In this study, simulation runs were carried out for the two sheet configurations depicted in Table 1. Sheet A, with $\Delta\bar{x} = \Delta\bar{y} = 0.1$, is a good approximation to the continuous case, as verified in the Results. The simulation conditions can be set by choosing arbitrarily either the cell size or the resistivity. Here we selected first a volume element, V_s, approximately equal to that of a single cell, and then proceeded to verify that the anisotropic resistivity values were realistic (see Electrical Parameters below). For simplicity, a constant value of $S_v = 0.2\ \mu m^{-1}$ was used in the calculations for both sheets A and B.

Sheet B has the same anisotropic resistivity values as sheet A, but different discretization factors ($\Delta\bar{x} = 0.1$, $\Delta\bar{y} = 0.3$). Using a larger $\Delta\bar{y}$ in sheet B provides a somewhat less accurate solution of Equations 6 and 7, the main feature being a deformation of the rising phase of the propagated action potential. This deformation is more or less pronounced according to the direction of propagation and is largest in the transverse direction. There are, therefore, substantial directional variations in $\dot{V}_{max}$ and τ_{foot} and negligible changes in V_{max} (Table 3). Among these factors, $\dot{V}_{max}$ stands to be the most potent to affect the transmembrane current (see Results and Discussion) and thereby the extracellular potential (Eq. 8). On the other hand, changes in τ_{foot} affect the time required for the depolarization to reach the firing threshold level and may be expected to be related to the propagation velocity, as is quite clear in the continuous case (Eq. A.15).

As indicated in Results, there are transient propagation phenomena occurring in the vicinity of the stimulation site and distortions near the borders of the sheet. In the present study, we have focused our attention on the situation where the propagation parameters are essentially

TABLE 1
Physical Dimensions of the Sheet Models

Physical dimension	Sheet A	Sheet B
Length Δx (μm)	80	80
Width Δy (μm)	20	60
Thickness h (μm)	10	10
No. of elements	131 × 96	131 × 32
Surface-to-volume ratio S_v (per μm)	0.2	0.2
Length constant (μm)		
Longitudinal, λ_x	800	800
Transverse, λ_y	200	200
Discretization factor		
Longitudinal, $\Delta\bar{x} = \Delta x/\lambda_x$	0.1	0.1
Transverse, $\Delta\bar{y} = \Delta y/\lambda_y$	0 1	0.3

Downloaded from http://ahajournals.org by on March 12, 2022

constant and steady state propagation may be presumed to exist. In practice, such a situation occurs at some 5 or 6 length constants away from the stimulation site and about 2 length constants from the borders.

Electrical Parameters

Values of the cell membrane capacitance, C_m, and the resting membrane resistance, R_m, are as given in Table 2. The resting potential, V_R, is −84.8 mV and the other parameters of the Beeler-Reuter model are as in Drouhard and Roberge (1982b).

The resistivity values indicated in Table 2 are in reasonable agreement with representative experimental measurements. The value of $\rho_e = 100\ \Omega\cdot$cm is close to that of a normal saline solution. For a plane wave propagating along the longitudinal axis of the cells, the total resistance contributed by each cell is given by

$$R_x = \rho_x \frac{\Delta x}{h\ \Delta y} = \rho_c \frac{\Delta x}{h\ \Delta y} + \frac{\rho_{jx}}{A_{jx}} \qquad (9)$$

and similarly for the transverse direction

$$R_y = \rho_y \frac{\Delta y}{h\ \Delta x} = \rho_c \frac{\Delta y}{h\ \Delta x} + \frac{\rho_{jy}}{A_{jy}} \qquad (10)$$

where $\rho_c(\Omega\cdot$cm) is the cytoplasmic resistivity, ρ_{jx} and ρ_{jy} ($\Omega\cdot$cm^2) are the junctional resistivities along the two major axes, A_{jx} and A_{jy} (cm^2) are the corresponding junctional areas of contact, and the other quantities are as previously defined (Tables 1 and 2).

A reasonable value of $\rho_c = 360\ \Omega\cdot$cm may be assumed. In the longitudinal direction, with $\rho_x = 488\ \Omega\cdot$cm and assuming a junctional area of contact equal to the cross-section of the cell (i.e., $A_{jx} = h\ \Delta y$), Equation 9 yields $\rho_{jx} = 1.0\ \Omega\cdot$cm^2. In the transverse direction, the average junctional area of contact might be assumed smaller since there is apparently a sparser distribution of lateral discs in comparison with intercalated discs (Spira, 1971). Assuming, for example, that $A_{jy} = 0.2\ A_{yx}$, the value of $\rho_y = 7800$ is seen to correspond (Eq. 10) to a transverse junctional resistivity (ρ_{jy}) of 0.74 $\Omega\cdot$cm^2 for sheet A and 2.2 $\Omega\cdot$cm^2 for sheet B. These figures are in good agreement with experimental observations (Chapman and Fry, 1978; Spach et al., 1982) and suggest that the resistivity values adopted here are not unreasonable.

For sustained propagation to occur in a cable or a sheet, the combined strength and duration of the stimulus must be such that a critical minimum number of elements become excited. In a cable, this is the liminal length for excitation (Rushton 1937) which is of the order of one length constant. The counterpart in two dimensions is a liminal area which has the form of an ellipse surrounding the stimulation point in the case of an anisotropic structure. Because of this situation, it is acceptable to distribute the applied stimulus current among several neighboring elements in order to reduce the required current intensity. In the present two-dimensional studies, propagation was elicited by applying a 0.25 msec pulse of 0.85 mA/cm^2 over several neighboring elements. The stimulated area comprised 5 × 5 elements in sheet A and 3 × 3 elements in sheet B, and was about five times smaller than the liminal area in both cases.

TABLE 2
Electrical Parameters of the Sheet Models

Electrical parameters	Sheet A or sheet B
C_m (μF/cm^2)	1.0
R_m ($\Omega\cdot$cm^2)	6250
ρ_x ($\Omega\cdot$cm)	488
ρ_y ($\Omega\cdot$cm)	7800
ρ_e ($\Omega\cdot$cm)	100
Stimulus amplitude (mA/cm^2)	0.85
Stimulus duration (msec)	0.25

The time of activation, at any given point of the sheet, is taken as the instant at which the action potential upstroke reaches 0 mV. The ray velocity, $\bar{\theta}_\beta$, is calculated from the time taken to cover one length constant along a radial line issuing from the stimulation site at an angle β from the horizontal axis (see Fig. 9).

The rising phase of the action potential is characterized by the parameters listed in Table 3. V_{max} and $\dot{V}_{max}$ are, respectively, the maximum amplitude and maximum rate of rise of the action potential, $V(\dot{V}_{max})$ and $t(\dot{V}_{max})$ are the voltage and time coordinates of $\dot{V}_{max}$, τ_{foot} and τ_{peak} are, respectively, the time constant of the foot of the action potential and the time constant of the upstroke as it approaches V_{max}. The magnitudes of V_{max} and $V(\dot{V}_{max})$ are measured from the resting potential level. The value of τ_{foot} was determined by fitting the expression $V_o - V_T = A\ \exp(t/\tau_{foot})$ to the foot of the action potential using a least-square procedure. The initial value, V_o, is fixed at 1 mV above the resting level. The first set of points used in the calculation comprises the first three potential values (0.032 msec apart) above V_o. Subsequent potential values are added one by one to constitute as many additional sets of points. The parameters (V_T, A, τ_{foot}) and the least-square residue are computed for each set of points. The parameter estimates remained fairly stable for a range of

TABLE 3
Parameters of the Rising Phase of the Action Potential in the Steady State

	Sheet A		Sheet B	
	Longitudinal	Transverse	Longitudinal	Transverse
V_{max} (mV)	97.1	97.0	96.8	94.9
$\dot{V}_{max}$ (mV/msec)	91.1	91.0	90.2	107.7
$V(\dot{V}_{max})$(mV)	56.5	56.5	58.3	66.9
$t(\dot{V}_{max})$(msec)	2.43	2 43	2 5	3 1
τ_{foot} (msec), measured	0.484	0.484	0.481	0.606
τ_{foot} (msec), computed	0 492	0 492		
τ_{peak} (msec)	0.327	0.327	0.337	0.235

Downloaded from http://ahajournals.org by on March 12, 2022

10–20 mV above the resting potential level, and it was verified that the maximum deviation for any individual point remained lower than 0.01 mV. We calculated τ_{peak} in the same way, starting from V_{max} as the initial potential value (V_0) and working backward along the time course of the upstroke.

Results

Throughout the Results, we use sheet A for the continuous medium case and sheet B for the case where the value of $\dot{V}_{max}$ varies according to the direction of propagation. The characteristics of these two models are compared with respect to intracellular events, propagation velocity, and extracellular potentials.

Intracellular Events during Propagation

The Action Potential

In the steady state, once the action potential waveform and the propagation velocity have stabilized, the rising phase of the action potential is the same in all directions in sheet A. This is verified in Table 3 where the listed action potential parameter values are practically identical in the longitudinal and transverse directions. This property corresponds to a uniform value of the discretization factors along both major axes of the sheet model (Table 1). As in the one-dimensional case (Joyner, 1982), the action potential waveform is not affected when a smaller value of the discretization factors is used.

In the model, the foot of the action potential upstroke and its peak as it approaches V_{max} can always be fitted well by exponential functions (both in sheets A and B) so the corresponding time constants, τ_{foot} and τ_{peak}, can be measured accurately (see Methods). The good correspondence between the computed (using Eq. A.15) and measured values of τ_{foot} attests to the validity of the assumptions used in deriving Equation A.15. The uniform values of the parameters of the rising phase of the action potential, including τ_{foot} and τ_{peak}, along the major axes (Table 3) and throughout sheet A supports the appropriateness of using it as a model of a continuous medium (see Appendix).

The situation is different in sheet B where the directional dependence of $\dot{V}_{max}$ corresponds to a non-uniform value of the discretization factors ($\Delta\bar{x} = 0.1$, $\Delta\bar{y} = 0.3$). Despite the fact that sheets A and B have equal $\Delta\bar{x}$ values, there are nevertheless minor differences in the rising phase of the action potential along the x-axis (Table 3). V_{max} and $\dot{V}_{max}$ are slightly reduced in sheet B while $V(\dot{V}_{max})$, $t(\dot{V}_{max})$, and the measured τ_{foot} and τ_{peak} are slightly increased. This point is taken up in the Discussion in conjunction with the corresponding changes in conduction velocity and extracellular potentials. However, the major differences between the action potential upstroke for sheets A and B are seen in the transverse direction (see Fig. 8). In comparison to the longitudinal direction, the action potential modifications in the transverse direction in sheet B are roughly as follows (Table 3): 2% decrease in V_{max}, 19% increase in $\dot{V}_{max}$, 15% increase in $V(\dot{V}_{max})$, 24% increase in $t(\dot{V}_{max})$, 24% increase in τ_{foot}, and 30% decrease in τ_{peak}.

These simulated conditions are comparable to experimental measurements on thin sheets of cardiac muscle. Spach et al. (1981) have reported the following differences between the transverse and longitudinal directions (see their Table 1): 6% increase in V_{max}, 38% increase in $\dot{V}_{max}$ and 27% decrease in τ_{foot}. These experiments also indicate an increase in $V(\dot{V}_{max})$ and a possible increase in $t(\dot{V}_{max})$ as the propagation velocity decreases (Spach, 1983; Fig. 7). Therefore there are satisfactory similarities between the conditions of the present simulation (sheet B) and the experimental observations on cardiac muscle, except for the changes in V_{max} and τ_{foot} which are in the wrong direction (see Discussion).

Isochrones and Velocity Profiles

Since the sheet model is composed of cells with identical membrane properties, the shape of the isochrones depends solely upon the directional resistance and possible directional differences in the shape of the action potential. Because of the uniform values of the discretization factor in sheet A, the action potential waveform is uniform throughout the sheet and the directional resistance constitutes the only determining element. For similar reasons, the velocity profile will be determined solely by the directional resistance. Therefore, in conformity with the continuous medium theory (see Appendix), both the isochrones and the velocity profile of sheet A are elliptical, with values of θ_x and θ_y (i.e. $\vec{\theta}_\beta$ at 0° and 90°, respectively) as given in Table 4. Indeed, as predicted by Equation A.17, we find $\theta_x/\theta_y = (\rho_y/\rho_x)^{1/2} = 4.0$. Values of the subthreshold velocity, $\vec{\theta}_{0\beta}$, calculated from Equation A.13, are also given in Table 4. The ratio of the actual and subthreshold propagation velocities is uniform throughout sheet A, in accord with the theory. Therefore, the characteristics of sheet A correspond very well to the continuous case.

Sheet B is different, as already noted for the shape of the rising phase of the action potential. Compared to sheet A, the propagation velocity is increased slightly in the longitudinal direction (about 1.6%) (Table 4), concomitantly with a reduction in $\dot{V}_{max}$ (see Discussion), but the major effect is a nonnegligible decrease in θ_y (about 7%). Deviations from the continuous case in sheet B are apparent when considering the ratio $\theta_x/\theta_y = 4.37$ (different from $(\rho_y/\rho_x)^{1/2} = 4.0$) and the non-uniform value of $|\vec{\theta}_\beta|/|\vec{\theta}_{0\beta}|$ for the major axes (Table 4).

It should be remarked that the concept of "passive" velocity (Appendix, Eqs. A.10 and A.13), as the ratio of the length constant to the membrane time constant, reflects only some of the fixed passive characteristics of the cell. Together with the discretization factor, it is useful to characterize the sheet model.

Downloaded from http://ahajournals.org by on March 12, 2022

TABLE 4
Propagation Parameters of the Sheet Models in the Steady State

	Sheet A		Sheet B	
	Longitudinal	Transverse	Longitudinal	Transverse
β (degrees)	0°	90°	0°	90°
θ_β (cm/sec)	43.9	11.0	44.6	10.2
$\theta_{\alpha\beta}$ (cm/sec)	12.8	3.2	12.8	3.2
$\lvert\theta_\beta\rvert / \lvert\theta_{\alpha\beta}\rvert$	3.43	3.43	3.48	3.19
ϕ_e (arbitrary units)				
Positive peak	0.0640	0.0032	0.0655	0.0032
Negative peak	−0.0595	−0.0192	−0.0582	−0.0179
Peak-to-peak	0.1235	0.0224	0.1237	0.0211
(grad V)$_{max}$ (mV/cm)	2007.1	7799.3	1924.5	5619.8

The isochrones obtained from sheets A and B are practically identical in shape, the only difference being a small degree of flattening in the transverse direction in sheet B due to the slightly reduced propagation velocity (Table 4). Figure 2 shows a set of isochrones obtained after the application of a stimulus near the lower lefthand corner of sheet B, at the origin of coordinates. The elliptic isochrone profile is established early despite the fact that steady state propagation occurs only several length constants away from the stimulation site (see Extracellular Potentials, below). Here, because of the small size of the sheet, edge effects are first seen on the lefthand side of the sheet, about one length constant from the border. Similar edge effects appear at the bottom of the sheet, starting with isochrone profile 4 (Fig. 2), and again within about one length constant from the border. Note that the boundary effects result in a small increase in the velocity of propagation in cells near the border. This is due to the fact that no current can flow out of the sheet, so that more current is available to flow in the direction parallel to the border and, hence, to accelerate propagation.

The Membrane and Axial Currents

It is of interest to see if the directional characteristics of the rising phase of the action potential in sheet B lead to differences in the time course of the sodium membrane current. Figure 3 compares the time courses of the ionic and capacitive currents during the action potential in the transverse direction for sheets A and B. There is practically no difference between the ionic current waveforms despite appreciable changes in the action potential parameters, as listed in Table 3. It appears, therefore, that the sodium conductance of the Beeler-Reuter model is not sufficiently sensitive to translate the actual differences in the action potential upstroke into ionic current changes.

There are, on the other hand, substantial differences between the transverse capacitive current waveforms of sheets A and B, while the longitudinal ones are essentially identical. As expected from the

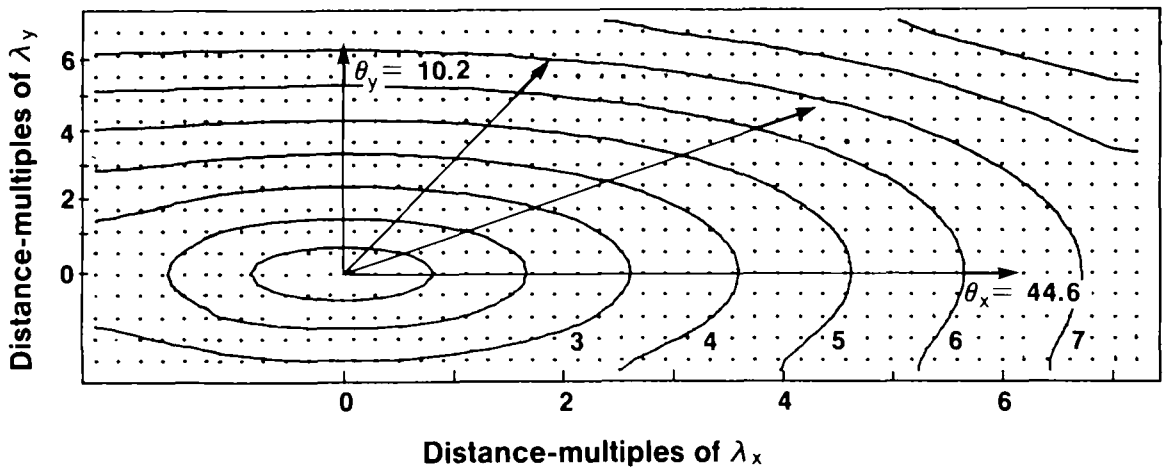

FIGURE 2. *Isochrone profiles obtained in sheet B. Only one of every two units is represented by a dot on the diagram, and only part of the sheet is shown. The stimulus was applied at the center of coordinates and gave rise to the elliptic profiles 1 through 7. The direction of the steady state ray velocity is indicated at 0°, 18.4°, 45°, and 90° from the horizontal axis (longitudinal cell direction).*

Downloaded from http://ahajournals.org by on March 12, 2022

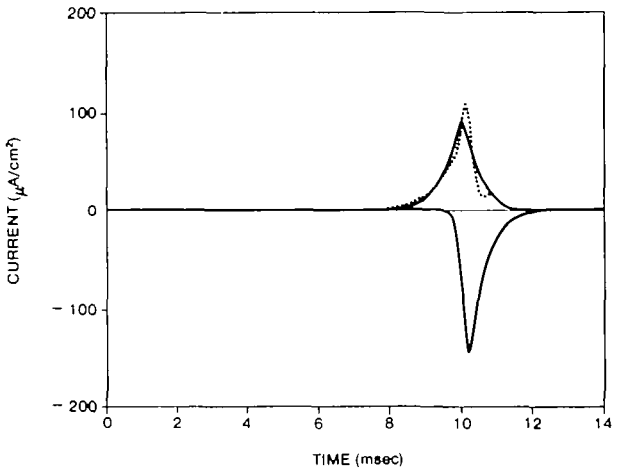

FIGURE 3. *Time course of capacitive (positive waveform) and ionic (negative waveform) currents during a propagated action potential in the transverse direction. Full lines correspond to sheet A and dotted line to sheet B. The ionic current waveforms in both sheets A and B were practically identical and have been superimposed here for purposes of time alignment.*

features of the action potential upstroke (Table 3), the transverse capacitive current rises more slowly during the foot of the action potential in sheet B (Fig. 3). Beyond the threshold level, the rise and fall of the capacitive current are much more rapid in sheet B. In accord with the data on $\dot{V}_{max}$ (Table 3), the peak capacitive current has a correspondingly larger value and a later time of occurrence. This behavior of the capacitive current in sheet B reflects the larger transverse discretization factor ($\Delta\bar{y} = 0.3$) whereby the distance between cell junctions is now 30% of the length constant, that is, three times the corresponding distance in sheet A. The net result is a looser coupling between adjacent units, despite the fact that the transverse resistivity is unchanged (Table 2). In other words, due to the greater width of the sheet elements, each one receives a comparatively lower amount of axial current from its neighbors [as can be inferred from the lower transverse value of $(\text{grad } V)_{max}$ in Table 4]. Thus, the behavior of the rising phase of the action potential in the transverse direction in sheet B is somewhat closer to the situation where the action potential does not propagate, and one of the consequences is a larger V_{max}.

During the foot of the action potential in the Beeler-Reuter model, the small membrane current consists of capacitive and time-independent potassium current components (Drouhard and Roberge, 1982b). Since the sodium current is activated only at threshold, the ionic current during the foot is very small. For example, below threshold, the relation $I_{ion} = V/Rm$, for an offset of 8 mV, gives a current of 1.28 $\mu A/cm^2$ flowing through $Rm = 6.25\ K\Omega \cdot cm^2$. This current is negligible in comparison with the peak ionic current during the action potential (Fig. 3). The expression derived for τ_{foot} in the Appendix (Eq. A.15) is valid in sheet A, since the conditions of uniform propagation are respected. It is not applicable to sheet B because the propagated action potential upstroke is not uniform throughout the sheet.

The diffusion of axial current is determined in the model by the local gradient of intracellular potential and the effective axial resistivity. The general shape of the distribution of intracellular potential with distance is as shown in Figure 4, where waveforms in the transverse direction are compared for sheets A and B. The amplitude corresponds to V_{max} and the main feature of interest is the maximum space derivative, $(\text{grad } V)_{max}$.

In the transverse direction, we expect to find a larger value of $(\text{grad } V)_{max}$ because of the much higher resistivity. As shown in Table 4, $(\text{grad } V)_{max}$ is nearly four times larger in the transverse than in the longitudinal direction in sheet A. In sheet B, however, the transverse $(\text{grad } V)_{max}$ value is only about three times larger than the longitudinal one. Note also a slight reduction (about 4%) of the longitudinal $(\text{grad } V)_{max}$ value in sheet B in comparison to sheet A.

Extracellular Potentials

Steady state propagation is achieved only at some distance from the stimulation site, and, in the meantime, there are changes in the action potential waveform, the propagation velocity, and the extracellular potential waveform. The development of the extracellular potential over the surface of the sheet is illustrated in Figures 5 and 6. In the longitudinal direction, the biphasic character of the wave is already established at one length constant from the stimulus site, and stability is achieved between 6 and 10 msec following stimulation (Fig. 5A). In the transverse direction, the potential remains largely negative (Fig. 5B) and stable propagation occurs

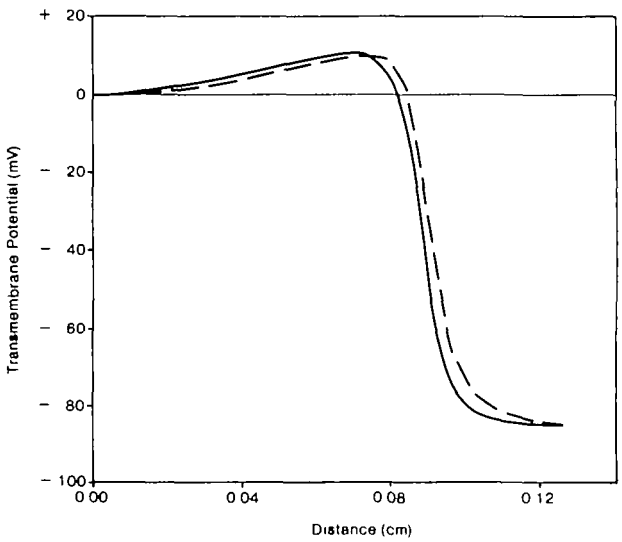

FIGURE 4. *Transverse intracellular potential gradients for sheet A (broken line) and sheet B (full line). The maximum values, $(\text{grad } V)_{max}$, are as given in Table 4.*

Downloaded from http://ahajournals.org by on March 12, 2022

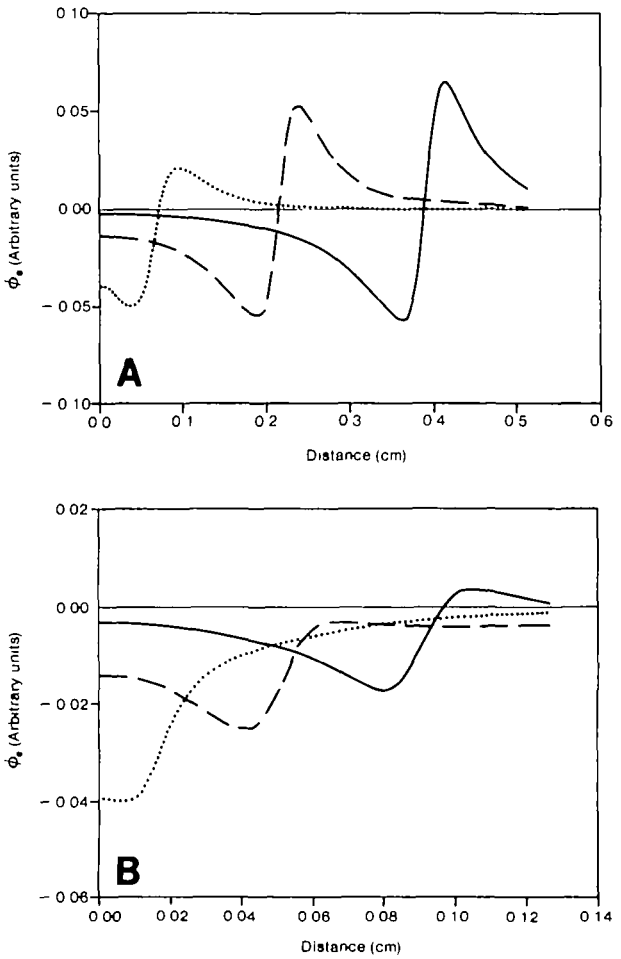

FIGURE 5. *Spatial distribution of the extracellular potential in sheet B at 2 (dotted line), 6 (broken line), and 10 msec (full line) following stimulation. Panel A corresponds to the longitudinal direction and panel B to the transverse direction. The abscissa gives the distance from the stimulation site. The extracellular potential amplitude is expressed in the same arbitrary units in Figures 5 through 8.*

after a delay of about 10 msec. For all practical purposes, events at 10 msec following stimulation correspond to a fairly well established steady state for the extracellular potential waveform, the propagation velocity, and the rising phase of the action potential.

A more complete description of the spatial extracellular potential distribution is shown in Figure 6 for sheet B. The isopotential contour map obtained at 10 msec after stimulation illustrates the effects of the anisotropic resistivity parameters chosen. The leading edge of the isochrone is represented by the heavy full line partly surrounding the stimulation site. The excitation wave is completely surrounded by positive potentials, although the magnitude is quite low in the transverse direction (see Fig. 5B). Large fluctuations (Fig. 5A) are confined to a small region around the x-axis (Fig. 6). The shape of this potential distribution is quite comparable to that described by Spach et al. (1979) at 9 msec following stimulation (see their Fig. 6).

In sheet A, the shape of the extracellular potentials is very similar to that shown in Figures 5 and 6 for sheet B. The essential differences are in the magnitude of the peak values, as indicated in Table 4. The peak-to-peak amplitudes are essentially equal in the longitudinal direction, whereas a decrease of about 6% is seen in the transverse direction in sheet B. It is seen in Figure 6 that the extracellular isopotential contours are much flattened in the transverse direction and are truly non-elliptical. This general shape is practically unaffected by the discretization.

In the time domain, the extracellular potential waveform is closely correlated with the propagation velocity and, thus, with the anisotropic resistivity. Large amplitude biphasic deflections occur in the longitudinal direction, where the propagation velocity is high, whereas triphasic waveforms of lower amplitude are seen in slow areas of the sheet. Figure 7A shows the extracellular potential obtained at 0.24 cm from the stimulation site in the longitudinal direction, at a distance of 60 μm from the sheet surface. The waveforms for sheets A and B are essentially identical, with practically no difference in the peak-to-peak amplitude. The differences between sheets A and B are more important in the transverse direction because of the differing discretization factors and $\dot{V}_{max}$ values. Waveforms shown

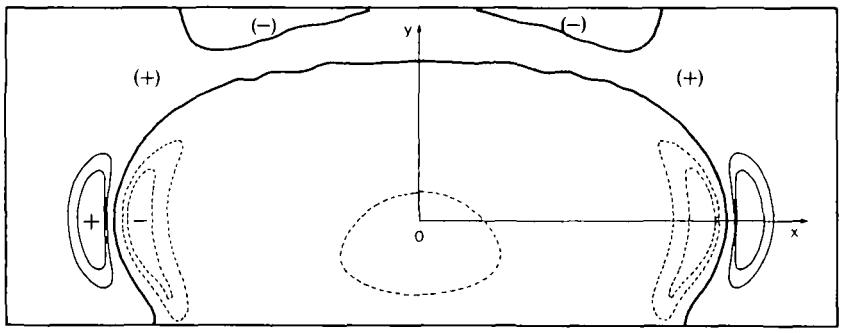

FIGURE 6. *Extracellular isopotential map for sheet B at 10 msec following stimulation. The sheet dimensions are 0 6 cm × 0.14 cm. It has been expanded by a factor of 2 in the transverse direction for illustrative purposes. The heavy full line is the zero potential level, and the regions of positive and negative potentials are as indicated. The finer full lines are the positive potentials (not shown in the transverse direction because of the low level, Fig. 5B). The broken lines are the negative potentials. Positive (+) and negative (−) extrema correspond to the peaks in Figure 5A (see also Table 4).*

Downloaded from http://ahajournals.org by on March 12, 2022

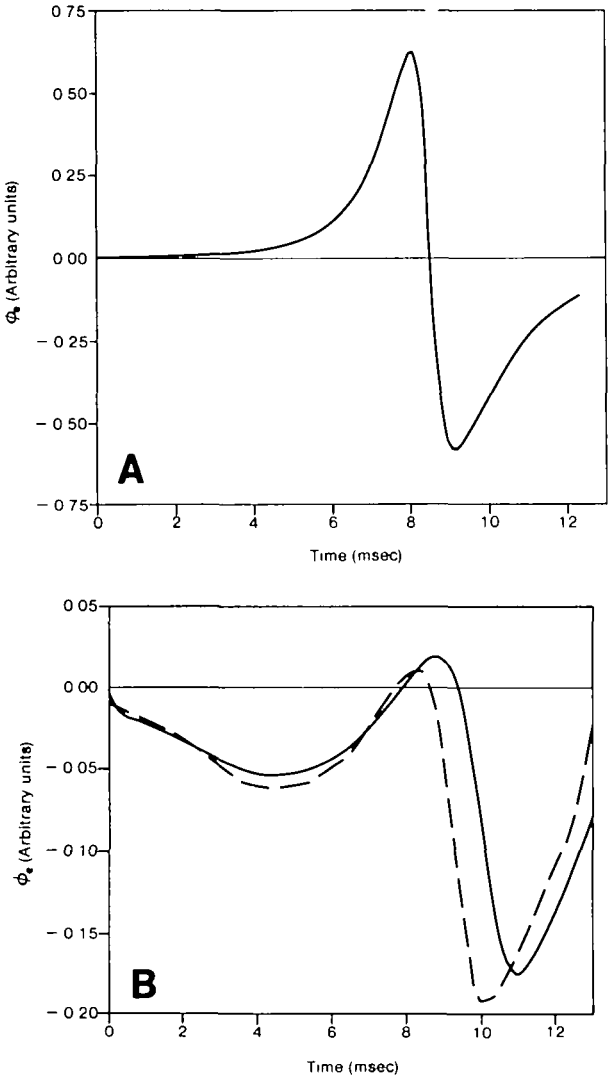

FIGURE 7. *Extracellular potential waveforms for propagation in the longitudinal (panel A) and transverse direction (panel B). The full and broken lines in panel B correspond to sheets A and B, respectively.*

in Figure 7B were obtained at 0.09 cm from the stimulation site, also at 60 μm from the sheet surface. In sheet B, the potential is slightly delayed due to the lower propagation velocity and is shifted upward so the positive portion of the waveform is relatively more important than in sheet A. The peak-to-peak amplitude is also a little smaller in sheet B (about 6%), as already indicated for the spatial extracellular potential.

It is of interest to consider the time alignment of the rising phase of the action potential and the corresponding extracellular potential waveform. For a given recording point along either axis, it was verified that $t(\dot{V}_{max})$ coincided with the maximum negative slope of the extracellular potential (intrinsic deflection). This is illustrated in Figure 8 for propagation in the transverse direction. For both sheets A and B, there is an exact coincidence between the time of the maximum rate of change of the intrinsic deflection and the value of $t(\dot{V}_{max})$ corresponding to the cell immediately underneath the recording site. A similar observation for the one-dimensional case has been reported by Spach and Kootsey (1985).

Discussion

In this study, we have used a numerical model in which the action potential is propagating actively in two dimensions, in a manner apparently analogous to the process occurring in real cardiac tissue. Although it was not attempted to duplicate exactly the relevant experimental observations, there is nevertheless quite good agreement for the range and spread of propagation velocities, as well as for the extracellular potential waveforms and distribution. The model can be made more realistic, as discussed below, with regard to the representation of the interstitial resistivity, the directional (or axial) resistivity, and the dynamics of the sodium membrane current, but these changes would not affect the qualitative features of the reconstructed dynamic events, and would introduce, for the most part, a substantial degree of complexity.

The major results of this paper are 3-fold. One is the satisfactory numerical solution of the continuous two-dimensional propagation equation and its use as an approximation of a continuous uniformly anisotropic medium. This solution is particularly useful to describe the shape and distribution of extracellular potentials in two-dimensions under idealized conditions of uniform intracellular anisotropic resistivity, constant electrical membrane properties, and constant propagated action potential waveform. Second, under the same conditions of uniform anisotropic resistivity and constant electrical membrane properties, we observe a limited sensitivity of the extracellular potentials and propagation velocity to directional changes in the rising phase of the action potential. Third, our results indicate that directional changes in $\dot{V}_{max}$ correspond to extracellular potential modifications, while directional changes in τ_{foot} are linked to the propagation velocity.

The Major Assumptions

One important simplifying assumption is the isotropicity and high conductivity of the interstitial space. This is equivalent to considering a single layer of cellular elements, each of which is in full contact with a large body of perfusing fluid. This choice was governed largely by practical consideration regarding the computer capacity and the computation time. We note, however, that when comparable conductivity values are used, a more exact representation of the anisotropic interstitial conductivity does not seem to give rise to qualitatively different propagation patterns (Barr and Plonsey, 1984).

Lumping together the cytoplasmic and junctional resistances of each cell and assuming that the resulting resistance is concentrated at the cell junction is another important simplification attached to the numerical solution. In the context of a large network

Downloaded from http://ahajournals.org by on March 12, 2022

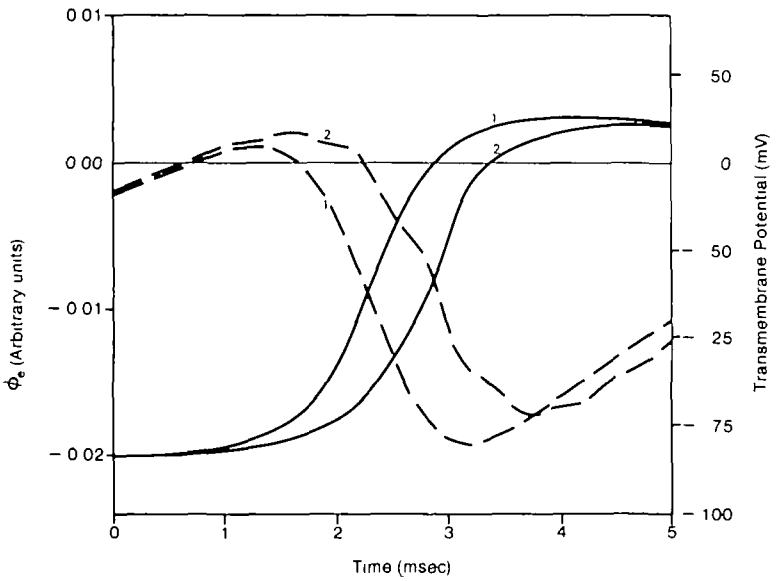

FIGURE 8. *Full lines are the rising phase of the action potential in the transverse direction in sheet A (curve 1) and in sheet B (curve 2). The scale on the righthand side of the illustration applies to the action potential. Broken lines correspond to transverse extracellular potential in sheets A (curve 1) and B (curve 2).*

study, and since little is known quantitatively about cellular junctions, this assumption about an average property of the cardiac tissue seems reasonable. The major consequence is the membrane isopotentiality of a given cell element or patch, that is the uniform polarization of the membrane area comprised between four adjacent intercellular connections. In view of the large sheet size, it seems that neglecting propagation over the surface of each small cell element cannot have great significance in the present context.

In the Methods, we have rationalized the choice of the resistivity values used in the model (Eqs. 9 and 10). The lack of reliable data on the total surface of the cell membrane and the surface area involved in intercellular connections leads to gross approximations which should eventually be revised. Using the parameters of Table 1, we can calculate a surface-to-volume ratio (S_v) of 0.33 μm^{-1} in sheet A and 0.26 μm^{-1} in sheet B. In doing so, we neglect the membrane infoldings, so S_v is likely to be underestimated. As a consequence, the length constants of the sheet would be correspondingly overestimated (Eq. 3). Here, by using $S_v = 0.2\ \mu m^{-1}$ for both sheets A and B, this overestimation is slightly more exaggerated.

The range of τ_{foot} values in the model is somewhat lower than in ventricular muscle, but larger than in atrial muscle (Spach et al., 1981). In the continuous case, Eqs. A.15 and A.16 indicate that τ_{foot} is determined by τ_m and the ratio $|\vec{\theta}_{0\beta}|/|\vec{\theta}_\beta|$. Since τ_m is a fixed parameter, the most practical way to change τ_{foot} is through the axial resistivity, $\vec{\rho}_\beta$, which also affects $\vec{\theta}_{0\beta}$ and $\vec{\theta}_\beta$. For example, as Equation A.17 indicates, a reduction of the axial resistivity would produce a shift of the whole range of propagation velocities towards higher values. This is desirable to a degree because the spread of velocities of 10–45 cm/sec in the model is lower than experimental measurements of 20–50 cm/sec (Spach et al., 1979).

The Beeler-Reuter membrane model used in this study is somewhat unsatisfactory with respect to its sodium current dynamics. A faster sodium current, such as in the Ebihara and Johnson (1980) model, would be desirable in order to have simulated $\dot{V}_{max}$ values closer to experimentally measured ones. Since the time constant of activation of the Beeler-Reuter model is already quite small (between 0.02 and 0.05 msec), the low $\dot{V}_{max}$ value is due mainly to the shallow steepness of the steady state activation curve and the rather small maximum sodium conductance (Beeler and Reuter, 1977). These conditions make the sodium conductance unresponsive to rapid changes in membrane potential during the upstroke, and only the capacitive and time-independent potassium currents are affected. This behavior explains the insensitivity of the extracellular potential to changes in $\dot{V}_{max}$ because the computation of ϕ_e as the integration of membrane current changes over a large number of cells (Eq. 8) tends to smooth out the relatively small changes in capacitive current (Fig. 3). Therefore, a model in which the sodium conductance is more responsive to rapid membrane potential changes could produce somewhat different results, although the resulting difference should not be expected to be too important in view of the integration process involved in Equation 8.

Injecting a strong current over a small surface area of the sheet forces a passive spread of axial current according to the sheet and cell membrane passive parameters. This current excites the neighboring cells, but sustained active propagation occurs only when a minimum number of cells around the stimulation site have been excited. This can be viewed as a liminal area for excitation in a two-dimensional structure, equivalent to the liminal length defined by Rushton (1937) for the propagation threshold in a cable. Once the propagation threshold has been reached, there are transient changes in the active

Downloaded from http://ahajournals.org by on March 12, 2022

potential waveform and propagation velocity over several length constants until a steady state is reached. These phenomena have not been specifically examined in the present stimulation study, except for the spatial distribution of extracellular potential shortly after stimulation (Fig. 5). We have restricted our attention to steady state propagation which was observed to occur some 5 or 6 length constants away from the stimulation site.

Propagation in a Uniform Anisotropic Sheet

When the longitudinal and transverse discretization factors are equal (sheet A), the shape of the propagated waveform is constant in all directions and we have a numerical model of a uniformly anisotropic, two-dimensional medium. Here the solution obtained with a value of 0.1 was found to be sufficiently accurate. For the activation from a localized stimulation focus (approximation of a point source of current), our results confirm or establish the following points:

(1) The resulting isochrones and propagation velocity profiles are elliptical, as predicted by the continuous theory (Eq. A.4). (2) The rising phase of the action potential, including τ_{foot}, has a constant shape in all directions. (3) The propagation velocity in any direction is inversely proportional to the square root of the directional resistivity, as predicted by the theory (Eq. A.17). (4) The ratio of the actual and subthreshold propagation velocities is constant in all directions, as predicted by the theory (Eq. A.14). (5) The extracellular isopotential field is non-elliptical, with an intensity closely correlated to the elliptical propagation velocity profile.

In contrast with the idealized anisotropic tissue model described by Barr and Plonsey (1984), the present model ignores the complexities of the interstitial resistive milieu. On the other hand, the representation of the tissue geometry and cellular interconnections in the numerical model is more realistic.

Non-Uniform Propagation

Sheet B, like sheet A, is uniform with respect to its anisotropic resistivity, and its electrical membrane properties are constant throughout. Nonuniform propagation occurs as a result of functional perturbations at the cell level in the form of directional differences in the upstroke of the action potential. Such directional effects were produced by an increase in the transverse discretization factor ($\Delta\bar{y}$), involving only an increase in the transverse cell size since the length constant was unchanged (Table 1). This manipulation produced propagation changes in the whole sheet, although the most conspicuous ones occurred in the transverse direction.

By increasing the transverse cell size 3-fold in sheet B we observe, in the transverse direction and in comparison with sheet A, an increase in $\dot{V}_{max}$ (about 18%), a decrease in $(\text{grad } V)_{max}$ (about 28%), an increase in τ_{foot} (about 24%), and slight decreases in velocity and extracellular potentials (Tables 3 and 4). In addition, we note a sizable perturbation of the capacitive current in sheet B while the ionic current is unaffected (Fig. 3). Despite the large reduction in $(\text{grad } V)_{max}$ (Table 4), Fig. 3 shows that the transverse capacitive current is increased transiently at its onset and at its peak. This is interpreted (see Results) as a virtual increase in the transverse resistance in sheet B which reduces somewhat the coupling between adjacent cells. As a consequence, there is some redistribution of the axial current flowing through the longitudinal and transverse junctions. More specifically, because of the apparent increase in the transverse resistance in sheet B, there is a small increase in the longitudinal current in comparison with the situation in sheet A.

The minor effects observed in the longitudinal direction in sheet B, in comparison with sheet A, can be explained on the basis of this small additional longitudinal current. The simplest way is to view this current increase as equivalent to a small virtual reduction in the longitudinal resistance. Because of the general relation between velocity and axial resistance (Eq. A.17), the slightly lower resistance induces a slightly higher velocity (Table 4). Comparison between the two major axes in sheet A shows that a higher velocity is paralleled by a lower $(\text{grad } V)_{max}$ and a larger extracellular potential amplitude (Table 4). Therefore, the changes in the longitudinal direction in sheet B [lower $(\text{grad } V)_{max}$ and larger ϕ_e amplitude] are concordant with a slight increase in velocity. Furthermore, all other things being equal, a decrease in $\dot{V}_{max}$ (Table 3) must follow this virtual decrease in axial resistance. This pattern of variations between velocity, $\dot{V}_{max}$ and extracellular potentials has been shown to be a fundamental characteristic of normal anisotropic heart muscle (Spach et al., 1981; Spach, 1982).

Under the conditions of the present study, it is clear that the extracellular potential modifications result from the directional changes in $\dot{V}_{max}$ through their effects on the capacitive membrane current (Fig. 3 and Eq. 8). A 19% increase in $\dot{V}_{max}$ between the longitudinal and transverse directions of the sheet produces a maximum decrease of about 6% in the peak-to-peak amplitude of the extracellular potential. It must be noted, however, that our model may be expected to underestimate the effects of directional changes in $\dot{V}_{max}$ on the extracellular potentials compared the situation which may be presumed to exist in cardiac muscle. One reason for this is the lower maximum variation in $\dot{V}_{max}$ in the model compared to cardiac muscle (19% vs. 38%). Another reason is the rather low basic value of $\dot{V}_{max}$ in the Beeler-Reuter model because of the slow sodium current dynamics. For example, comparing the longitudinal $\dot{V}_{max}$ in the model with $\dot{V}_{max}$ in cardiac tissue for the highest propagation velocity, we have about 90 V/sec (Table 3) vs. 124 V/sec in ventricular muscle and 161 V/sec in atrial muscle (Spach et al., 1981, Table 1).

The obvious discrepancy of the present numerical

Downloaded from http://ahajournals.org by on March 12, 2022

model is the fact that the changes in the transverse τ_{foot} and V_{max} in sheet B are in the wrong direction compared to experimental observations (Spach et al., 1981). In the present study a 24% increase in τ_{foot} was accompanied by a small decrease (about 7%) in the transverse propagation velocity. This result is in general agreement with the continuous medium theory (Eq. A.15). Then, it is reasonable to surmise that the decrease in the transverse τ_{foot} in cardiac tissue may be associated with a relative increase in the transverse propagation velocity. As far as we know, there are no data available to test that prediction. We cannot account for the deficiency of the numerical model with respect to the direction of variation in τ_{foot} and V_{max}, and it is likely that new or modified assumptions are required. Similar observations were made on the basis of one-dimensional simulation studies (Joyner, 1982; Spach, 1983).

In an earlier study, Spach et al. (1979) noted that the extracellular potentials computed using a constant action potential shape were close to those recorded experimentally in a thin sheet of cardiac tissue. The present results extend this observation by showing, under conditions of active propagation, that directionally different shapes of the action potential upstroke have a limited influence on the computed extracellular potentials. More generally, the results obtained with sheet B suggest that functional perturbations at the microscopic level, unaccompanied by perturbations of either the net axial resistivity or cell membrane properties cannot lead to very substantial changes in the macroscopic variables. Perturbations of the anisotropic resistivity of the sheet would have direct and powerful effects on the propagation velocity (viz. Eq. A.17) and, presumably, on the extracellular potential also. Studies on abnormal cardiac tissue provide an extreme illustration of the effects to be expected. In 2-month old infarcts, action potentials in a thin layer of muscle neighboring the infarcted tissue are close to normal, while the myocardial structure is highly disorganized as a result of connective tissue invasion (Ursell et al., 1985). Under these conditions, the isochrone patterns deviate drastically from the elliptical shape, and the extracellular potentials show wide variations in amplitude and a variable degree of fragmentation.

Appendix

Two-Dimensional Continuous Medium Theory

In a resistive two-dimensional anisotropic conducting medium, the relation between the current density, $\vec{J}$, and the electric field, $\vec{E}$, follows Ohm's law

$$\vec{J} = \sigma\vec{E}$$

where σ is a symmetric conductivity tensor of order 2 (Landau and Lifshitz, 1960). Using coordinates parallel to the principal directions of the tensor, the latter can be expressed in diagonal form as

$$\sigma = \begin{bmatrix} \sigma_x & 0 \\ 0 & \sigma_y \end{bmatrix} \quad (A.2)$$

and Eq. A.1 becomes

$$J_x = \sigma_x E_x; \quad J_y = \sigma_y E_y \quad (A.3)$$

where σ_x and σ_y are the axial conductivities along the x-axis and y-axis, respectively, relating the corresponding current density components, J_x and J_y, and electric field components, E_x and E_y. These axial conductivities enter into the two-dimensional propagation equation (Eq. 2) as $\rho_x = 1/\sigma_x$ and $\rho_y = 1/\sigma_y$ (see Eq. 3).

For the activation, from a point source, of the system described by the two-dimensional propagation equation (Eq. 2), the work of Muler and Markin (1977) shows that the resulting isochrones are elliptical. Under conditions of steady state propagation, the velocity profile is also elliptical since the length of the radius vector of the isochrone is proportional to the ray velocity, $\vec{\theta}_\beta$. As indicated in Fig. 9, $\vec{\theta}_\beta$ is the propagation velocity along a radius vector at an angle β with the longitudinal axis. Thus, we have

$$|\vec{\theta}_\beta| = \theta_x\theta_y[\theta_y^2\cos^2\beta + \theta_x^2\sin^2\beta]^{-1/2} \quad (A.4)$$

where θ_x and θ_y are the propagation velocities along the longitudinal and transverse directions, respectively. These assumptions give also

$$\frac{\lambda_x}{\theta_x} = \frac{\lambda_y}{\theta_y} = \frac{|\vec{\lambda}_\beta|}{|\vec{\theta}_\beta|} = \text{constant} \quad (A.5)$$

with the length constants λ_x and λ_y (see Eqs. 2 and 3) defined along the major axes. λ_β is the length constant in the direction of $\vec{\theta}_\beta$. By analogy with Equation 3, we have

$$|\vec{\lambda}_\beta| = (R_m/|\vec{\rho}_\beta|S_v)^{1/2} \quad (A.6)$$

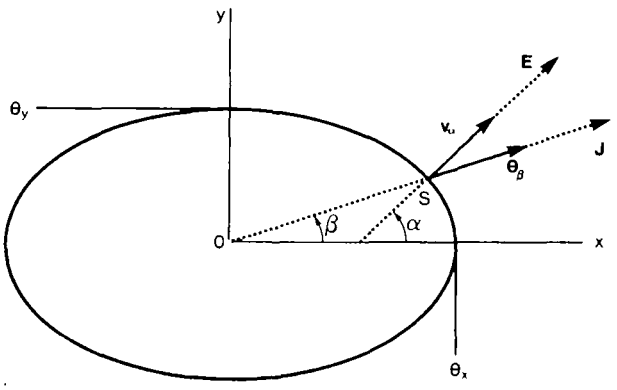

FIGURE 9. *Illustration of a theoretical elliptic velocity profile resulting from stimulation at the center of coordinates in a continuous anisotropic medium (Eq. 2) θ_x and θ_y are the maximum and minimum velocities, respectively, and are related through Equation A.4 for conditions of constant propagation velocity. $\vec{\theta}_\beta$ is the ray velocity (Eq. A.4) and $\vec{v}_n$ the normal velocity (Eq. A 8) $\vec{E}$ and $\vec{J}$ are the potential gradient and current density vectors, respectively, for an isochrone coinciding with the elliptic velocity profile shown.*

Downloaded from http://ahajournals.org by on March 12, 2022

with

$$|\vec{\rho}_\beta| = \rho_x \cos^2\beta + \rho_y \sin^2\beta \qquad (A.7)$$

where $\vec{\rho}_\beta$ is the resistivity in the direction of $\vec{\theta}_\beta$.

Within a small region centered at point S, Figure 9, the velocity normal to the isochrone (or to the velocity distribution profile), $\vec{v}_\alpha$, corresponds to a flat wavefront. We have

$$|\vec{v}_\alpha| = |\vec{\theta}_\beta| \cos(\beta - \alpha). \qquad (A.8)$$

It should be noted that the electric field $\vec{E}$ is normal to the isochrone at point S, and is therefore co-linear with $\vec{v}_\alpha$ (Fig. 9). However, the current density $\vec{J}$ is a radial vector co-linear with $\vec{\theta}_\beta$. Thus, the definition of a radial resistivity, $\vec{\rho}_\beta$, is arbitrary outside the major axes since $\vec{J}$ and $\vec{E}$ are not co-linear.

During the foot of the action potential, when the membrane potential is close to the resting potential, the membrane can be regarded as passive and linear. The ionic part of the membrane current under these conditions is simply $I_{ion} = V/R_m$. Equation 2 then becomes a linear differential equation

$$\lambda_x^2 \frac{\partial^2 V}{\partial x^2} + \lambda_y^2 \frac{\partial^2 V}{\partial y^2} - \tau_m \frac{\partial V}{\partial t} - V = 0 \qquad (A.9)$$

It can be seen that λ_x and λ_y appear as the natural units of length in the passive sheet (Eq. A.6) and τ_m the natural unit of time. This leads us to regard

$$\theta_{ox} = \lambda_x/\tau_m; \quad \theta_{oy} = \lambda_y/\tau_m \qquad (A.10)$$

as natural expressions of the conduction velocity at the subthreshold level along the two major axes.

In the adimensional system described by Equation 4, the steady state propagation of a constant waveform is described by Helmholtz's equation (Mathews and Walker, 1965). In our original coordinate system, this condition can be expressed as:

$$\theta_x^2 \frac{\partial^2 V}{\partial x^2} + \theta_y^2 \frac{\partial^2 V}{\partial y^2} = \frac{\partial^2 V}{\partial t^2}. \qquad (A.11)$$

Substituting Equations A.5 and A.11 into Equation A.9 gives the following equation for the early foot of the action potential

$$\left(\frac{|\vec{\lambda}_\beta|}{|\vec{\theta}_\beta|}\right)^2 \frac{\partial^2 V}{\partial t^2} - \tau_m \frac{\partial V}{\partial t} - V = 0. \qquad (A.12)$$

By analog with Equation A.7, we can write the expression for the conduction velocity at the subthreshold level in the direction of $\vec{\theta}_\beta$ as

$$|\vec{\theta}_{o\beta}| = |\vec{\lambda}_\beta|/\tau_m \qquad (A.13)$$

Combining Equations A.5, A.7, and A.10, we find

$$\frac{\theta_x}{\theta_{ox}} = \frac{\theta_y}{\theta_{oy}} = \frac{|\vec{\theta}_\beta|}{|\vec{\theta}_{o\beta}|} = \text{constant} \qquad (A.14)$$

which indicates that the ratio of the actual and subthreshold conduction velocities is constant in a uniform sheet.

Equation A.12 has a solution of the form $V(t) = V_o \exp(t/\tau_{foot})$, where

$$\tau_{foot} = \frac{2\tau_m}{(|\vec{\theta}_\beta|/|\vec{\theta}_{o\beta}|)^2 (1 + \sqrt{1 + 4(|\vec{\theta}_{o\beta}|/|\vec{\theta}_\beta|)^2})} \qquad (A.15)$$

The time constant of the foot of the action potential, τ_{foot}, is therefore determined by the time constant of the membrane and the ratio of the actual and subthreshold conduction velocities. Therefore, τ_{foot} has a constant value throughout a uniform and continuous two-dimensional medium.

When $\vec{\theta}_\beta \gg \vec{\theta}_{o\beta}$, Equation A.12 gives the following approximation

$$\tau_{foot} = \tau_m \left(\frac{|\vec{\theta}_{o\beta}|}{|\vec{\theta}_\beta|}\right)^2 \qquad (A.16)$$

which yields, using Equations A.10 and A.13,

$$|\vec{\theta}_\beta|^2 = K/|\vec{\rho}_\beta| \qquad (A.17)$$

where K is a constant since τ_{foot} and all the other parameters involved are also constant.

All the software programs for this project were written by Alain Vinet. We gratefully acknowledge the free computer time allowed to this project by the Centre de Calcul of the University of Montreal.

This work was supported by the Medical Research Council and the Natural Sciences and Engineering Research Council of Canada, and the Quebec Heart Foundation.

Address for reprints: Fernand A. Roberge, Institut de Génie Biomédical, Université de Montréal, P.O. Box 6128, Station A, Montreal (Quebec), Canada H3C 3J7.

Received April 9, 1984; received in revised form July 3, 1985; accepted for publication January 13, 1986.

References

Barr RC, Plonsey R (1984) Propagation of excitation in idealized anisotropic two-dimensional tissue. Biophys J **45:** 1191–1202

Beeler GW, Reuter H (1977) Reconstruction of the action potential of ventricular myocardial fibres. J Physiol (Lond) **268:** 177–210

Chapman RA, Fry CH (1978) An analysis of the cable properties of frog ventricular myocardium. J Physiol (Lond) **283:** 263–282

Clerc L (1976) Directional differences of impulse spread in trabecular muscle form mammalian heart. J Physiol (Lond) **255:** 335–346

Crank J, Nicholson P (1947) A practical method for numerical evaluation of solutions of partial differential equations of the heat-conduction type. Proc Cambridge Phil Soc **43:** 50–67

Drouhard JP, Roberge FA (1982a) The simulation of repolarization events of the cardiac Purkinje fiber action potential. IEEE Trans Biomed Eng **29:** 481–493

Drouhard JP, Roberge FA (1982b) A simulation study of the ventricular myocardial action potential. IEEE Trans Biomed Eng **29:** 494–502

Forsythe GE, Wasow WR (1960) Finite difference methods for partial differential equations. New York, J Wiley, p 236

Geselowitz DB, Barr RC, Spach MS, Miller WT III (1982) The impact of adjacent isotropic fluids on electrogram from anisotropic cardiac muscle. A modeling study. Circ Res **51:** 602–613

Hodgkin AL (1954) A note on conduction velocity. J Physiol (Lond) **125:** 221–224

Jack JJB, Noble D, Tsien RW (1975) Electric Current Flow in Excitable Cells. Oxford, Clarendon Press

Joyner RW (1982) Effects of the discrete pattern of electrical

Downloaded from http://ahajournals.org by on March 12, 2022

coupling on propagation through an electrical syncytium. Circ Res **50:** 192–200
Joyner RW, Ramon F, Moore JW (1975) Simulation of action potential propagation in an inhomogeneous sheet of coupled excitable cells. Circ Res **36:** 654–661
Joyner RW, Veenstra R, Rawling D, Chorro A (1984) Propagation through electrically coupled cells. Biophys J **45:** 1017–1025
Landau LD, Lifshitz EM (1960) Electrodynamics of Continuous Media. New York, Pergamon Press
Mathews J, Walker RL (1965) Mathematical Methods in Physics. New York, Benjamin Co.
Moore JW, Ramon F (1974) On numerical integration of the Hodgkin and Huxley equations for a membrane action potential. J Theor Biol **45:** 249–273
Muler AL, Markin VS (1977) Electrical properties of anisotropic nerve-muscle syncitia. III. Steady form of the excitation front. Biophysics **22:** 699–704
Plonsey R (1969) Bioelectric Phenomena. New York, McGraw-Hill
Plonsey R, Barr RC (1984) Current flow patterns in two-dimensional anisotropic bysyncitia with normal and extreme conductivities. Biophys J **45:** 557–571
Plonsey R, Rudy Y (1980) Electrocardiogram sources in a 2-dimensional anisotropic activation model. Med Biol Eng Comp **18:** 87–94
Roberts D, Hersh LT, Scher AM (1979) Influence of cardiac fiber orientation on wavefront voltage, conduction velocity, and tissue resistivity in the dog. Circ Res **44:** 701–712
Rushton WAH (1937) Initiation of the propagated disturbance. Proc R Soc Lond [Biol] **124:** 210–243
Spach MS (1982) The electrical representation of cardiac muscle based on discontinuities of axial resistivity at a microscopic and macroscopic level. *In* Normal and Abnormal Conduction in the Heart, edited by A Paes de Carvalho, BE Hoffman, M Lieberman. Mount Kisco, N.Y., Futura, pp 145–179
Spach MS (1983) The discontinuous nature of electrical propagation in cardiac muscle. Ann Biomed Eng **11:** 207–261
Spach MS, Kootsey JM (1985) Relating the sodium current and conductance to the shape of transmembrane and extracellular potentials by simulation. Effects of propagation boundaries. IEEE Trans Biomed Eng **BME-32:** 743–755
Spach MS, Miller WT III, Miller-Jones E, Warren RB, Barr RC (1979) Extracellular potentials related to intracellular action potentials during impulse conduction in anisotropic canine cardiac muscle. Circ Res **45:** 188–204
Spach MS, Miller WT III, Geselowitz DB, Barr RC, Kootsey JM, Johnson EA (1981) The discontinuous nature of propagation in normal canine cardiac muscle. Evidence for recurrent discontinuities of intracellular resistance that affect the membrane currents. Circ Res **48:** 39–54
Spach MS, Kootsey JM, Sloan JD (1982) Active modulation of electrical coupling between cardiac cells of the dog. A mechanism for transient and steady state variations in conduction velocity. Circ Res **51:** 347–362
Spira AW (1971) The nexus of the intercalated disc of the canine heart: Quantitative data for the estimation of its resistance. J Ultrastruct Res **34:** 409–425
Ursell PC, Gardner PI, Albala A, Fenoglio JJ, Wit AL (1985) Structural and electrophysiological changes in the epicardial border zone of canine myocardial infarcts during infarct healing. Circ Res **56:** 436–451
Victorri B, Vinet A, Roberge FA, Drouhard JP (1985) Integration methods for action potential reconstruction using Hodgkin-Huxley-Type models. Comp Biomed Res **18:** 10–23
Woodbury JW, Crill WE (1961) On the problem of impulse conduction in the atrium. *In* Nervous Inhibition, edited by E Florey. New York, Pergamon Press, pp 124–135

INDEX TERMS: Two-dimensional propagation • Cardiac action potential • Cardiac extracellular potential • Cardiac muscle anisotropy • Propagation model

Downloaded from http://ahajournals.org by on March 12, 2022